Author Query Form

AUTHOR QUERIES - TO BE ANSWERED BY THE CORRESPONDING AUTHOR

The following queries have arisen during the typesetting of your manuscript. Please answer these queries by marking the required corrections at the appropriate point in the text.

Q1	Please consider rephrasing the sentence "However, the system is non-dissipative ..." for clarity.	
Q2	Please provide the publisher location for Refs. (4), (8), (17).	
Q3	Please provide the publisher location and page range for Ref. (16).	
Q4	Please provide the year of publication for Ref. (19).	

ON THE BUCKLING OF ELASTIC PLATES

by N. J. BALMFORTH *and* A. C. SLIM

(*Department of Mathematics, University of British Columbia,* 1984 *Mathematics Road, Vancouver, British Columbia* V6T 1Z2*, Canada*)

N. J. BALMFORTH

(*Department of Earth and Ocean Science, University of British Columbia,* 6339 *Stores Road, Vancouver, British Columbia* V6T 1Z4*, Canada*)

and

R. V. CRASTER[†]

(*Department of Mathematics, Imperial College London, South Kensington Campus, London* SW7 2AZ)

Summary

The Föppl–von Kármán equations are used to explore the onset of linear instability and the subsequent nonlinear development of buckling patterns in a flat elastic plate due to an imposed shear or body force such as gravity. Experimental results are also presented for a clamped and sheared sheet of Neoprene rubber and these compare favourably to theory.

1. Introduction

A classical problem in elasticity is the buckling of a flat plate under the influence of a compressive stress (**1**). In the conventional formulation of the problem, the stress is applied by compressing the clamped edges of the plate. However, one can also buckle the plate by shearing the edges or by introducing a body force like gravity directed within the plane of the plate. Despite a variety of important applications in the engineering sciences and elsewhere, these latter buckling scenarios have received much less attention and motivate the present study.

The buckling of a uniformly sheared, clamped plate was considered by Southwell and Skan (**2**) who used linear stability theory of a flat plate to derive a criterion for the onset of buckling in terms of the imposed shear stress. Subsequent experiments (**3**) largely confirmed the predictions, once material imperfections were taken into account. Beyond Southwell and Skan's analysis, developments of shear-induced buckling have remained relatively sparse, aside from a related body of work on the wrinkling of membranes in which bending stiffnesses are either relatively insignificant or small (for example (**4** to **6**)). By contrast, in the current article we consider plates with significant bending stiffness, which lends for a more transparent and complete exploration of the onset and development of buckling patterns as the degree of shear increases. In fact, the wrinkled membrane can be considered as the asymptotic limit of strong shear in the buckling problem studied here. Thus, effectively, we fill in the gap between the onset of buckling and the strongly sheared wrinkled membrane.

[†] ⟨ r.craster@imperial.ac.uk ⟩

The buckling of a clamped plate under gravity has apparently not been considered previously, although vertically suspended, laterally compressed membranes were studied by (**7**), and there are common points with what one might call the 'drapes problem', in which a hanging curtain develops arcing folds stemming from points where it is tethered (**8**). Our own interest in body-forced buckling arose from a number of analogous applications in which a flowing fluid current tugs from beneath on an elastic surface layer. A primary application of such elastic-plated gravity currents is to the wrinkling and folding of the solidifying surface layers of lava flow (**9**).

Our approach to the problem is a mix of theory and experiment. To describe the phenomenon mathematically, we use the nonlinear plate equations of von Kármán and Föppl (**1**, **10**). These equations are a popular model for finite deformations of plates that incorporate geometric nonlinearities, while retaining a linear constitutive law (for example (**11**, **12**)). We complement this theory with a suite of experiments on a sheet of Neoprene rubber. A sliding frame is used to impose a controlled amount of shear on the clamped sheet, thereby allowing us to detect the onset of instability and explore pattern formation for shear-induced buckling. Though comprising a far cruder and less controlled experiment, we also used the same sheet to verify that gravity can also buckle the sheet when it is clamped to a frame and stood up vertically.

In section 2, we begin by formulating the problem in terms of the governing Föppl–von Kármán equations. We then consider linear stability of a flat plate (section 3), extending the original results of (**2**). Linear stability theory is limited in that it captures only the dynamics of infinitesimally small perturbations, and there is a danger that finite-amplitude patterns may appear below the linear onset (subcritically). In section 4, we rule this possibility out and show that nonlinear buckling can be expected only above the linear onset (that is, the bifurcation to buckling patterns is supercritical), and then construct the patterns that smoothly appear from the flat base state using weakly nonlinear theory. We then extend the results into the fully nonlinear regime using numerical solutions of the full, steady Föppl–von Kármán equations (section 5). For the uniform shear case, we present an asymptotic analysis for large shear (section 6) which dovetails with the work of Wong and Pellegrino (**6**, **13**, **14**). We present a comparison of the theoretical results with experiments in section 7 and conclude in section 8.

2. Formulation

Consider an elastic plate of half thickness d, density ρ, Poisson ratio ν and Young's modulus E. The undeformed plate lies in a plane described by coordinates $\tilde{\mathbf{X}} = (\tilde{X}, \tilde{Y})$ and is clamped along parallel edges at $\tilde{Y} = \pm Y_0$. The plate is subjected to uniform shear by a $2\xi_0$ relative displacement of the clamped edges parallel to their direction (Fig. 1a) or is suspended in a vertical plane and subject to gravity of magnitude g (Fig. 1b). In both cases, the shear may be supplemented by compressive or tensile forces resulting from a relative displacement of $2\eta_0$ of the clamped edges perpendicular to their direction in the plane of the plate.

The governing Föppl–von Kármán equations are given by

$$\tilde{\nabla} \cdot \tilde{\mathsf{N}} = 2\rho g d \begin{pmatrix} -\cos\theta \\ \sin\theta \end{pmatrix}, \quad 2\rho d \frac{\partial^2 \tilde{\zeta}}{\partial \tilde{t}^2} + \frac{2d^3 E}{3(1-\nu^2)} \tilde{\nabla}^4 \tilde{\zeta} = \tilde{\nabla} \cdot (\tilde{\mathsf{N}} \cdot \tilde{\nabla} \tilde{\zeta}), \tag{1}$$

where $\tilde{t}$ is the time, $\tilde{\nabla} = (\partial/\partial \tilde{X}, \partial/\partial \tilde{Y})$ and $\tilde{\nabla}^4 = (\partial^2/\partial \tilde{X}^2 + \partial^2/\partial \tilde{Y}^2)^2$, and the angle θ is the inclination of the plate edges with respect to gravity (see Fig. 1b). The in-plane stresses are

$$\tilde{\mathsf{N}} = \frac{2dE}{1-\nu^2} [\nu \operatorname{tr}(\tilde{\mathsf{e}})\mathsf{I} + (1-\nu)\tilde{\mathsf{e}}], \tag{2}$$
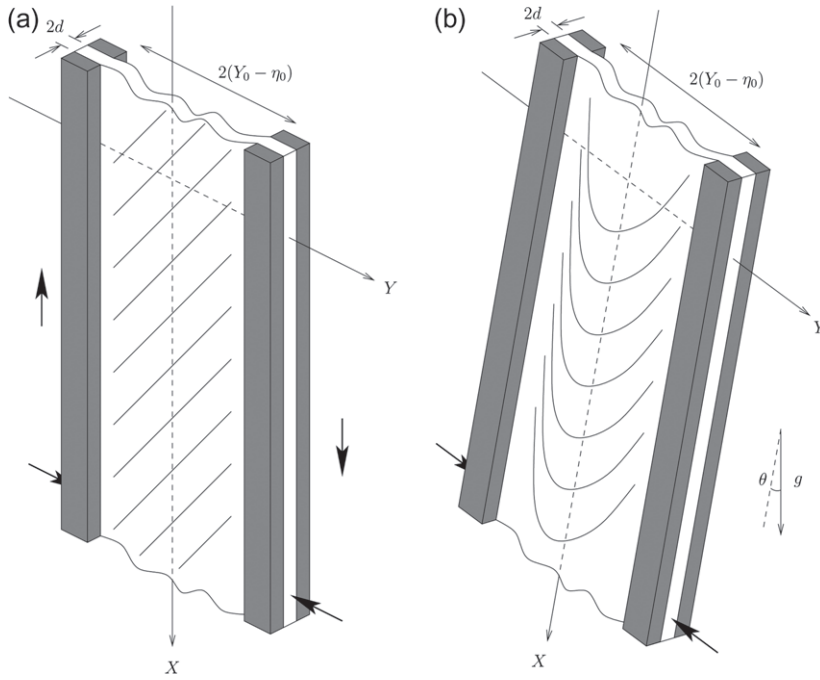
Fig. 1 The two configurations considered: (a) a plate with uniform shear induced by the relative displacement of the clamped edges along their length and (b) a plate suspended in a vertical plane

with associated strains

$$\tilde{\mathsf{e}} = \frac{1}{2}(\tilde{\boldsymbol{\nabla}}\tilde{\boldsymbol{\xi}} + \tilde{\boldsymbol{\nabla}}\tilde{\boldsymbol{\xi}}^{\dagger} + \tilde{\boldsymbol{\nabla}}\tilde{\zeta}\tilde{\boldsymbol{\nabla}}\tilde{\zeta}), \tag{3}$$

where $\tilde{\boldsymbol{\xi}} = (\tilde{\xi}, \tilde{\eta})$ is the in-plane displacement, $\mathrm{tr}(\cdot)$ denotes the trace, $\dagger$ the transpose and I the identity.

The plate is clamped at its edges and subjected to prescribed displacements:

$$\tilde{\xi} = \pm\xi_0, \quad \tilde{\eta} = \pm\eta_0, \quad \tilde{\zeta} = \frac{\partial\tilde{\zeta}}{\partial\tilde{Y}} = 0 \quad \text{at } \tilde{Y} = \pm Y_0. \tag{4}$$

In $\tilde{X}$, we impose periodic boundary conditions, adopting a domain of length $\tilde{L}$.

2.1 *Non-dimensionalization*

We remove dimensions from the equations and identify the important dimensionless parameters by introducing

$$\tilde{\mathbf{X}} = \mathbf{X}Y_0, \quad \tilde{t} = t\sqrt{\frac{(1-\nu^2)\rho Y_0^4}{Ed^2}}, \quad \tilde{\boldsymbol{\xi}} = \boldsymbol{\xi}\frac{d^2}{Y_0}, \quad \tilde{\zeta} = \zeta d, \quad \tilde{\mathsf{N}} = \mathsf{N}\frac{2d^3 E}{Y_0^2(1-\nu^2)}, \quad \tilde{\mathsf{e}} = \mathsf{e}\frac{d^2}{Y_0^2}.$$

The governing equations (1) now become

$$\nabla \cdot \mathsf{N} = \mathcal{G} \begin{pmatrix} -\cos\theta \\ \sin\theta \end{pmatrix}, \quad \frac{\partial^2 \zeta}{\partial t^2} + \frac{1}{3}\nabla^4 \zeta = \nabla \cdot (\mathsf{N} \cdot \nabla \zeta), \tag{5}$$

with

$$\mathsf{N} = \nu \operatorname{tr}(\mathsf{e})\mathsf{I} + (1-\nu)\mathsf{e}, \quad \mathsf{e} = \frac{1}{2}(\nabla\boldsymbol{\xi} + \nabla\boldsymbol{\xi}^\dagger + \nabla\zeta\nabla\zeta). \tag{6}$$

The boundary conditions (4) reduce to

$$\xi = \pm\mathcal{S}/(1-\nu), \quad \eta = \pm\mathcal{T}, \quad \zeta = \frac{\partial\zeta}{\partial Y} = 0 \quad \text{at } Y = \pm 1, \tag{7}$$

plus periodicity in X with period L.

In addition to the scaled domain length (the aspect ratio) L and Poisson ratio ν, three further dimensionless parameters appear:

$$\mathcal{S} = (1-\nu)\frac{\xi_0 Y_0}{d^2}, \quad \mathcal{T} = \frac{\eta_0 Y_0}{d^2}, \quad \mathcal{G} = \frac{\rho g(1-\nu^2)Y_0^3}{d^2 E}, \tag{8}$$

which provide measures of the shear, tension and relative magnitude of gravitational and elastic forces, respectively.

2.2 *Base state and perturbation equations*

The equations admit the X-independent, flat solution

$$\xi = \xi_b = \frac{(1-Y^2)\mathcal{G}\cos\theta + \mathcal{S}Y}{1-\nu}, \quad \eta = \eta_b = \frac{1}{2}\mathcal{G}\sin\theta(Y^2 - 1) + \mathcal{T}Y, \quad \zeta = \zeta_b = 0, \tag{9}$$

having associated stresses

$$\mathsf{N}_b = \begin{bmatrix} \nu(Y\mathcal{G}\sin\theta + \mathcal{T}) & \mathcal{S}/2 - Y\mathcal{G}\cos\theta \\ \mathcal{S}/2 - Y\mathcal{G}\cos\theta & Y\mathcal{G}\sin\theta + \mathcal{T} \end{bmatrix}. \tag{10}$$

By setting

$$\boldsymbol{\xi} = \boldsymbol{\xi}_b + \hat{\boldsymbol{\xi}}, \quad \zeta = \hat{\zeta}, \quad \mathsf{N} = \mathsf{N}_b + \hat{\mathsf{N}}, \quad \mathsf{e} = \mathsf{e}_b + \hat{\mathsf{e}}, \tag{11}$$

where the subscript b refers to the base state (9), we find that the perturbations, identified by the $\hat{\cdot}$ notation, satisfy

$$\nabla \cdot \hat{\mathsf{N}} = \mathbf{0}, \quad \frac{\partial^2 \hat{\zeta}}{\partial t^2} + \frac{1}{3}\nabla^4 \hat{\zeta} = \nabla \cdot (\mathsf{N}_b \cdot \nabla\hat{\zeta}) + \nabla \cdot (\hat{\mathsf{N}} \cdot \nabla\hat{\zeta}), \tag{12}$$

with the perturbed stresses and strains obeying (6). The clamped boundary conditions become

$$\hat{\xi} = \hat{\eta} = \hat{\zeta} = \frac{\partial\hat{\zeta}}{\partial Y} = 0 \quad \text{at } Y = \pm 1. \tag{13}$$

3. Linear stability analysis

To determine when the flat base state becomes unstable to infinitesimal perturbations, we linearize (12b) and decompose the displacement into normal modes, $\hat{\zeta} = Z(Y)\exp(ikX - i\omega t) + \text{c.c.}$, obtaining the eigenvalue problem

$$\frac{d^4Z}{dY^4} - (2k^2 + 3\mathcal{G}Y\sin\theta + 3\mathcal{T})\frac{d^2Z}{dY} + 3(2ikY\mathcal{G}\cos\theta - ik\mathcal{S} - \mathcal{G}\sin\theta)\frac{dZ}{dY}$$
$$+ [k^4 + 3k^2\nu(\mathcal{T} + \mathcal{G}Y\sin\theta) + 3ik\mathcal{G}\cos\theta]Z = 3\omega^2 Z, \qquad (14)$$

subject to

$$Z = \frac{dZ}{dY} = 0 \quad \text{at } Y = \pm 1.$$

Here, c.c. denotes the complex conjugate, k is the wave number (an integer multiple of $2\pi/L$ in our periodic domain) and ω is the frequency. Due to the self-adjoint character of the linearized form of (12b), ω^2 is real (2). Thus, if $\omega^2 < 0$ the mode grows exponentially; we solve (14) numerically to detect any such instabilities, varying k and the four parameters $\mathcal{S}, \mathcal{G}, \theta$ and $\mathcal{T}$ but fixing $\nu = 0.46$.

We first extend Southwell and Skan's results for the case of pure shear. Contours of the largest values of ω^2 over all normal modes are shown on the $(k, \mathcal{S})$-plane in Fig. 2a. Above the bold neutral stability curve, normal modes are unstable. Onset occurs at $\mathcal{S} = \mathcal{S}_c = 14\cdot8$ and $k = k_c = 1\cdot9$. For shear values above $\mathcal{S}_c$, there is an increasingly wide window of unstable modes at intermediate wave numbers. Contours of the out-of-plane displacement are plotted at four values of $\mathcal{S}$ for the most unstable wave number in Fig. 2(b) to (e).

Analogous results for the purely gravitational case are shown in Fig. 3; in this example $\theta = 0$ and the edges of the plate are purely vertical. Gravity then pulls the plate downwards, inducing a shear profile across the sheet that causes buckling at sufficiently large $\mathcal{G}$. Onset occurs for $\mathcal{G} = \mathcal{G}_c = 29\cdot2$ and $k = k_c = 2\cdot1$. Displacement profiles take the form of downward-directed chevrons. Close to onset the maximum displacement occurs at $Y = 0$, but as $\mathcal{G}$ is increased and the wavelength decreased, the maximum displacement shifts towards the clamped edges where there is most shear.

The stability boundaries shown in Figs 2 and 3 have asymptotes for large and small wave numbers that can be calculated analytically. For $k \gg 1$, a local analysis can be performed in which derivatives are replaced by local wave numbers, treating spatially dependent coefficients as constants, and then maximizing the resulting growth rate over that wave number. For $k \ll 1$, a standard long-wave expansion furnishes the result.

When the plate is inclined with respect to gravity, so that its edges are no longer vertical ($\theta \neq 0$), onset occurs at $\mathcal{G}_c = \mathcal{G}_c(\theta)$ and $k_c = k_c(\theta)$, as shown in Fig. 4. Inclining the plate generates compression against the lower edge promoting buckling at lower values of $\mathcal{G}_c$. Purely compressive buckling against the lower edge is ultimately favoured once θ becomes sufficiently large. Indeed, the critical wave number passes to zero at a critical inclination of about $60°$, at which point the problem reduces to a version of the Euler column with clamped edges, and $\mathcal{G}_c \sin\theta \approx 14\cdot73$. Thus, as we incline the plate, we proceed from a situation in which gravitationally induced shear drives buckling (at $\theta = 0$) to a purely compressive buckling (when $\theta > 60°$). Since the former is the more novel, from hereon we focus on non-inclined plates with $\theta = 0$.

Figure 5 illustrates the effect of combining shear- or gravity-driven buckling with either compression or tension. In tension, greater forces are required to instigate buckling, whereas in compression, less force is required. Where the critical curves intersect the $\mathcal{S}_c = k_c = 0$ or $\mathcal{G}_c = k_c = 0$ axes in
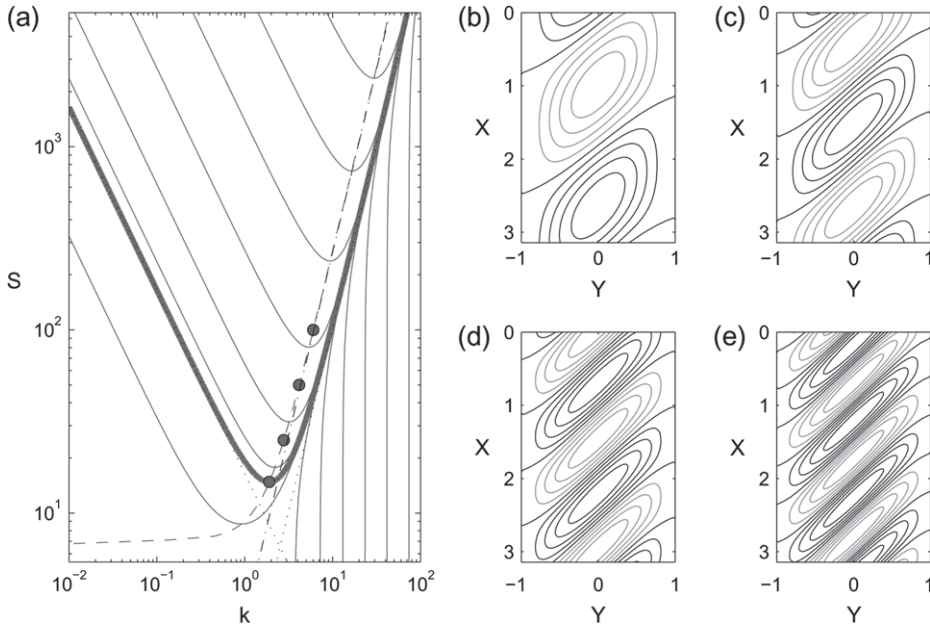
Fig. 2 Uniform shear-induced buckling ($\mathcal{T} = 0$). (a) Contours of constant ω^2 with values $\pm 10^j$, $j = 1, \ldots, 7$, on the $(k, \mathcal{S})$-plane. The bold solid curve indicates the stability boundary; dotted lines show the low- and high-wave number approximations $\mathcal{S} \approx 16 \cdot 4/k$ and $\mathcal{S} \approx 8k^2/3$. The dashed curve indicates the wave number having minimum ω^2 for given $\mathcal{S}$; as shown by the dashed-dotted line, this curve is approximately $\mathcal{S} \approx 16\sqrt{3}k^2/27$ for large k. Right-hand panels: out-of-plane displacement profiles on the (X, Y)-plane for the most unstable modes at (b) $\mathcal{S} = 14 \cdot 8$, (c) 25, (d) 50 and (e) 100. Contours are equally spaced in increments of $0 \cdot 2$ of the maximum amplitude

Fig. 5(a) and (c), compression alone produces instability according to the usual Euler beam threshold (here given by $\mathcal{T} = -\pi^2/3$).

4. The onset of buckling

4.1 *Buckling is supercritical*

Multiplying (12a,b) by $\hat{\xi}_t$ and $\hat{\zeta}_t$, respectively, and then integrating over the domain, we obtain the conservation law

$$\frac{d\mathcal{E}}{dt} = \frac{d}{dt}(\langle \hat{\zeta}_t^2 \rangle + \mathcal{E}_L + \mathcal{E}_N) = 0, \tag{15}$$

where

$$\mathcal{E}_L = \left\langle \frac{1}{3}(\nabla^2 \hat{\zeta})^2 + \nabla \hat{\zeta} \cdot \mathbf{N}_b \cdot \nabla \hat{\zeta} \right\rangle, \quad \mathcal{E}_N = \left\langle (1 - \nu) \sum_{i,j} (\hat{e}_{ij})^2 + \nu \operatorname{tr}(\hat{\mathbf{e}})^2 \right\rangle \tag{16}$$
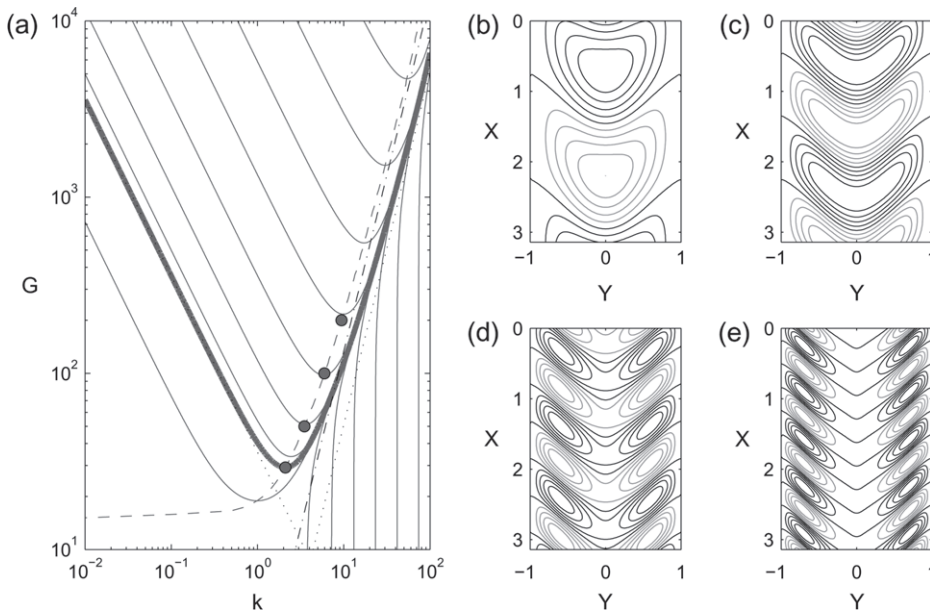
Fig. 3 Gravity-induced buckling ($\mathcal{T} = \theta = 0$). (a) Contours of constant ω^2 with values $\pm 10^j$, $j = 1, \ldots, 7$, on the $(k, \mathcal{S})$-plane. The bold solid curve indicates the stability boundary; dotted lines show the low- and high-wave number approximations $\mathcal{G} \approx 35\cdot6/k$ and $\mathcal{G} \approx 4k^2/3$. The dashed curve indicates the wave number having minimum ω^2 for given $\mathcal{S}$; as shown by the dashed-dotted line, this curve is approximately $\mathcal{G} \approx 8\sqrt{3}k^2/27$ for large k. Right-hand panels: out-of-plane displacements on the (X, Y)-plane for the most unstable modes at (b) $\mathcal{G} = 29\cdot2$, (b) 50, (c) 100 and (d) 200. Contours are equally spaced by increments of $0\cdot2$ of the maximum amplitude

and

$$\langle \cdot \rangle = \frac{1}{2L} \int_{-1}^{1} \int_{0}^{L} \cdot\, dX dY. \tag{17}$$

145   If all the constituents of $\mathcal{E}$ are positive definite, a perturbation cannot grow beyond some value specified by its initial condition. For a non-dissipative system such as the one we consider, this is equivalent to saying that the system is nonlinearly (neutrally) stable.

   In (15), the kinetic energy term, $\langle \hat{\zeta}_t^2 \rangle$, and the term arising from nonlinear contributions, $\mathcal{E}_N$, are both positive definite; only the term arising from linear contributions, $\mathcal{E}_L$, is sign indefinite. Thus,
150   the system is nonlinearly stable whenever $\mathcal{E}_L > 0$. This leads us to consider the variational problem of determining the minimum of the functional

$$\mathcal{F} = \left\langle \frac{1}{3}(\nabla^2 \hat{\zeta})^2 + \boldsymbol{\nabla}\hat{\zeta} \cdot \mathsf{N}_b \cdot \boldsymbol{\nabla}\hat{\zeta} \right\rangle - \Lambda(\langle \hat{\zeta}^2 \rangle - 1), \tag{18}$$

over all possible $\hat{\zeta}$ that satisfy the boundary conditions. Because $\mathcal{E}_L$ is purely quadratic, the variational problem is homogeneous and has a unique solution only once we include the normalization $\langle \hat{\zeta}^2 \rangle = 1$ via the Lagrange multiplier Λ (in other words, one must remove the arbitrary scaling of $\hat{\zeta}$).
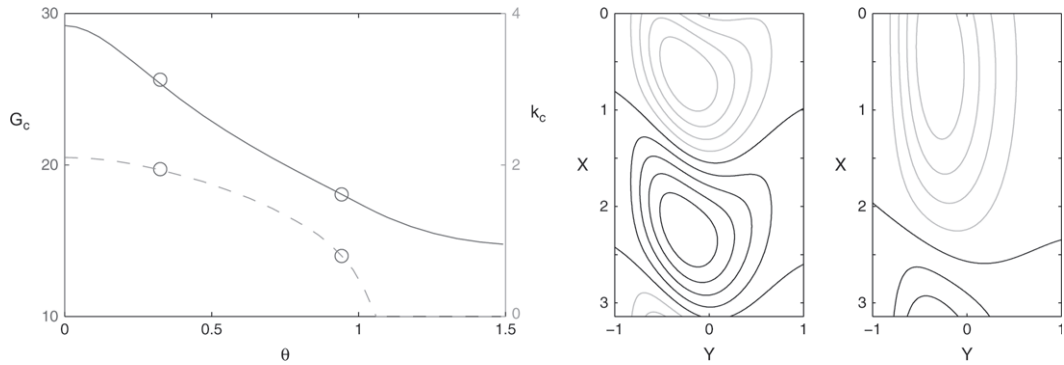
Fig. 4 $\mathcal{G}_c$ and k_c for varying inclinations of the plate with respect to gravity θ for $\nu = 0.46$ and $\mathcal{T} = 0$. Two out-of-plane displacements are shown in the right two panels and correspond to the positions on the neutral curves of the first panel indicated by circles
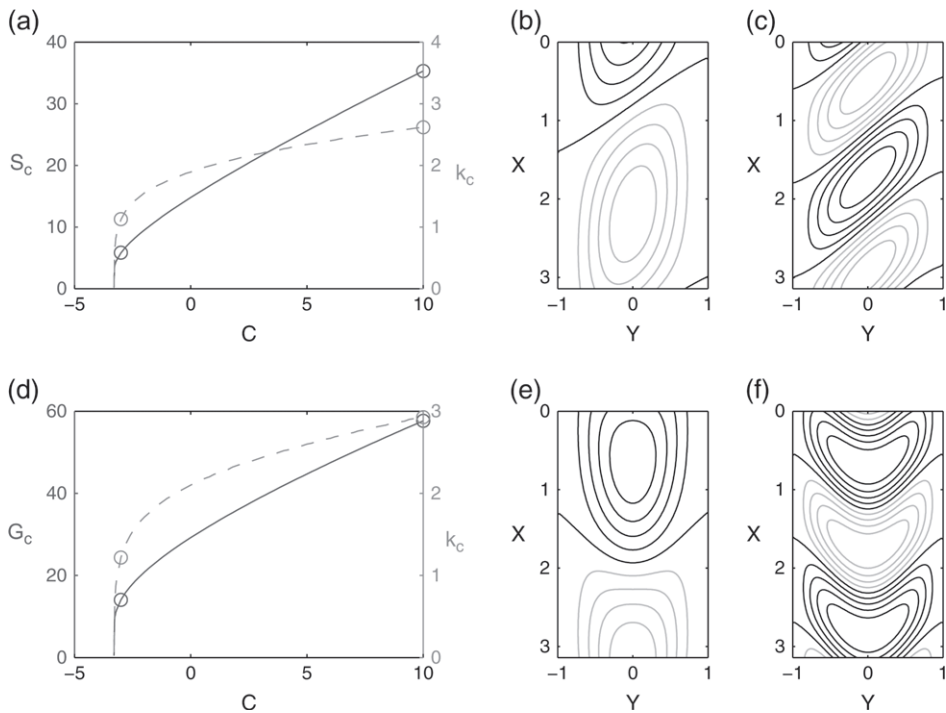

Fig. 5 Critical k and (a) $\mathcal{S}$ or (d) $\mathcal{G}$ with $\theta = 0$, for varying tension or compression $\mathcal{T}$ with $\nu = 0.46$. Four out-of-plane displacement profiles are shown on the right in panels (b), (c), (d) and (e) and correspond to the points shown by circles in the left-hand panels

155   The Euler–Lagrange equation associated with the minimization of $\mathcal{F}$ is

$$-\Lambda\hat{\zeta} + \frac{1}{3}\nabla^4\hat{\zeta} = \nabla \cdot (\mathsf{N}_b \cdot \boldsymbol{\nabla}\hat{\zeta}), \tag{19}$$

and the minimum value of $\mathcal{F}$ is Λ. Hence, provided $\Lambda > 0$, the system is nonlinearly stable. But (19) is precisely the linear stability equation (14) with $\Lambda \equiv \omega^2$. Thus, linear stability implies nonlinear stability, and buckled states cannot exist below the linear onset, ruling out subcritical bifurcations.

160   ## 4.2   *Weakly nonlinear analysis*

To find the slightly buckled (supercritical) states that appear just above the linear onset, we turn to weakly nonlinear theory. The overall vision is that we may tune the system to be on the brink of instability, with the domain size chosen so that there is a normal mode with wave number k_c and the shear or gravity parameter selected close to the relevant critical value, $\mathcal{S}_c$ or $\mathcal{G}_c$. A slight increase in
165   that parameter then places the system in the unstable regime where the distinguished normal mode becomes unstable and grows to finite, but low amplitude. The calculation is a standard one (for example (**15**, **16**)) and is formalized as an asymptotic expansion, using a small parameter $\epsilon \ll 1$. We set

$$\mathsf{N}_b = \mathsf{N}_b^{(0)} + \epsilon^2\mathsf{N}_b^{(2)}, \quad \frac{\partial}{\partial t} = \epsilon\frac{\partial}{\partial T} + \cdots, \quad \hat{\zeta} = \epsilon\hat{\zeta}^{(1)} + \epsilon^3\hat{\zeta}^{(3)} + \cdots,$$

$$\hat{\boldsymbol{\xi}} = \epsilon^2\hat{\boldsymbol{\xi}}^{(2)} + \cdots, \quad \hat{\mathsf{N}} = \epsilon^2\hat{\mathsf{N}}^{(2)} + \cdots, \quad \hat{\mathsf{e}} = \epsilon^2\hat{\mathsf{e}}^{(2)} + \cdots. \tag{20}$$

The expansion of the base state stresses, $\mathsf{N}_b = \mathsf{N}_b^{(0)} + \epsilon^2\mathsf{N}_b^{(2)}$, reflects the development of either $\mathcal{S}$
170   or $\mathcal{G}$ as $\mathcal{S}_c + \epsilon^2$ or $\mathcal{G} = \mathcal{G}_c + \epsilon^2$, respectively.

By substituting (20) into (12) and equating terms of equal order in ϵ, we find that, at leading order ϵ, the out-of-plane equation becomes

$$\mathcal{L}\hat{\zeta}^{(1)} \equiv \frac{1}{3}\nabla^4\hat{\zeta}^{(1)} - \nabla \cdot (\mathsf{N}_b^{(0)} \cdot \boldsymbol{\nabla}\hat{\zeta}^{(1)}) = 0, \tag{21}$$

with solution

$$\hat{\zeta}^{(1)} = A(T)e^{ik_cX}Z(Y) + \text{c.c.}, \tag{22}$$

where $A(T)$ is the currently undetermined amplitude and $Z(Y)$ is the eigenfunction of the marginally
175   stable normal mode. To remove any ambiguity in these definitions, we scale the eigenfunction so that $\max(|Z(Y)|) = 1/2$ or, equivalently, $\max(|\zeta^{(1)}|) = |A|$.

At order ϵ^3, the in-plane equation yields

$$\nabla \cdot \hat{\mathsf{N}}^{(2)} = 0, \tag{23}$$

which can be decomposed into linear differential equations for $\hat{\xi}^{(2)}$ and $\hat{\eta}^{(2)}$, forced by quadratic nonlinearities in $\hat{\zeta}^{(1)}$. Because of the form of $\hat{\zeta}^{(1)}$, the solutions can be written formally as

$$\hat{\boldsymbol{\xi}}^{(2)} = [A^2e^{2ik_cX}\hat{\boldsymbol{\xi}}_2^{(2)}(Y) + \text{c.c.}] + |A|^2\hat{\boldsymbol{\xi}}_2^{(0)}(Y), \tag{24}$$

where the vector $\hat{\boldsymbol{\xi}}_2^{(0,2)} = (\hat{\xi}_2^{(0,2)}, \hat{\eta}_2^{(0,2)})$.

At the same order, the out-of-plane equation gives

$$\mathcal{L}\hat{\zeta}^{(3)} = -\frac{\partial^2 \hat{\zeta}^{(1)}}{\partial T^2} + \nabla \cdot (\mathbf{N}_b^{(2)} \cdot \nabla \hat{\zeta}^{(1)}) + \nabla \cdot (\hat{\mathbf{N}}^{(2)} \cdot \nabla \hat{\zeta}^{(1)}). \tag{25}$$

Multiplying (25) by $Z^* e^{-ik_c X}$, where superscript $*$ indicates complex conjugate, and integrating over the domain, leads us to a solvability condition which demands that $A(T)$ satisfy the amplitude equation

$$\varpi \frac{\partial^2 A}{\partial T^2} = \kappa A - |A|^2 A, \tag{26}$$

where

$$\varpi = \frac{1}{I}\langle|Z|^2\rangle, \quad I = \frac{1}{|A|^4}\left\langle (1-\nu)\sum_{i,j}(\hat{e}_{ij}^{(2)})^2 + \nu\,\mathrm{tr}(\hat{\mathbf{e}}^{(2)})^2 \right\rangle \tag{27}$$

and

$$\kappa = \frac{1}{I}\left\langle ik_c N_{bXY}^{(2)}\left(\frac{dZ}{dY}Z^* - Z\frac{dZ^*}{dY}\right) - k_c^2 N_{bXX}^{(2)}|Z|^2 - N_{bYY}^{(2)}\left|\frac{dZ}{dY}\right|^2 \right\rangle. \tag{28}$$

Equation (26) has the form of a conservative nonlinear oscillator and solutions for a general initial condition are limit cycles. The non-dissipative form results from the neglect of damping in the Föppl–von Kármán equations and is not realistic in any practical application. The introduction of small dissipation into the problem generically causes the solutions of (26) to decay towards the fixed point $|A| = \sqrt{\kappa}$. This solution is also that expected if the conservative system was slowly brought into the unstable regime by gradually increasing the shear or introducing the body force (in the manner of a slow passage through a supercritical bifurcation). Whence, we argue that the relevant solution is the steady state, $|A| = \sqrt{\kappa}$ (a tighter argument requires a dissipative extension of the Föppl–von Kármán equations, which we do not attempt here; related arguments are made in (**15**)). Thus, κ, which is plotted against Poisson ratio in Fig. 6 for the uniform shear and gravity
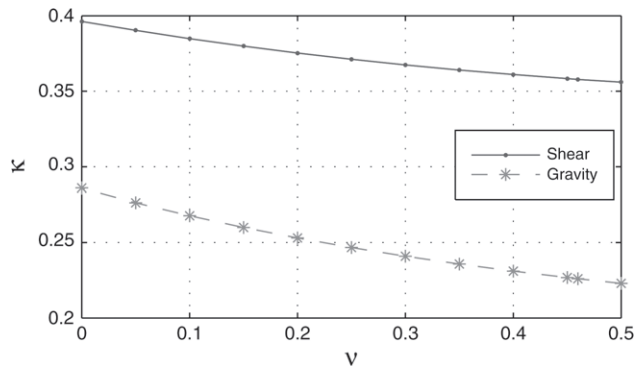

Fig. 6 The coefficient, κ, of the weakly nonlinear amplitude equation (26), against Poisson ratio, for the two cases of pure shear and gravity (with no inclination, $\theta = 0$ and $\mathcal{T} = 0$)

cases, determines how the buckle amplitude bifurcates from the base state with increasing $\mathcal{S}$ or $\mathcal{G}$:
$\epsilon|A| \equiv \sqrt{\kappa(\mathcal{S} - \mathcal{S}_c)}$ or $\sqrt{\kappa(\mathcal{G} - \mathcal{G}_c)}$.

5. Steady nonlinear solutions

5.1 *Amplitude and shape*

The weakly nonlinear solutions remain valid only in a small window of parameter space near onset. To continue those solutions into the fully nonlinear regime, we return to the Föppl–von Kármán equations and compute steady solutions numerically in domains of length $2\pi/k_c$. To accomplish the task, we reduce the problem to an algebraic one by using pseudospectral collocation and spectral differentiation matrices (**17**) with a periodic Fourier grid in X and a Chebyshev basis in Y, and then using Newton–Raphson iteration to find the function values at the gridpoints. Solutions are constructed first near linear onset, where the weakly nonlinear prediction provides an accurate initial guess, and continuation then maps out the solution branches beyond.

By analogy with weakly nonlinear theory, we define the buckle amplitude as the maximum value of the out-of-plane displacement over the spatial domain: $\epsilon A = \max(|\hat{\zeta}|)$. Figures 7 and 8 show computed buckle amplitudes for the pure shear- and gravity-driven cases, respectively. Also shown in the figures are sample displacement fields, which are not qualitatively different from the shapes predicted by weakly nonlinear theory over the parameter regime computed. In fact, the out-of-plane displacement is relatively close to the linear normal mode shape.

Figures 7 and 8 display the nonlinear states which appear when the plate first becomes unstable. However, an increase in $\mathcal{S}$ or $\mathcal{G}$ also leads to the appearance of additional finite-amplitude solutions with more wavelengths in the periodic domain. The new solutions appear when the normal modes of the base state with higher wave number, $k = Jk_c$ with $J = 2, 3, \ldots$, become unstable; we refer to the new solutions as the 'Jth' buckling states (for example, in the shear-driven case, the $2k_c$ and
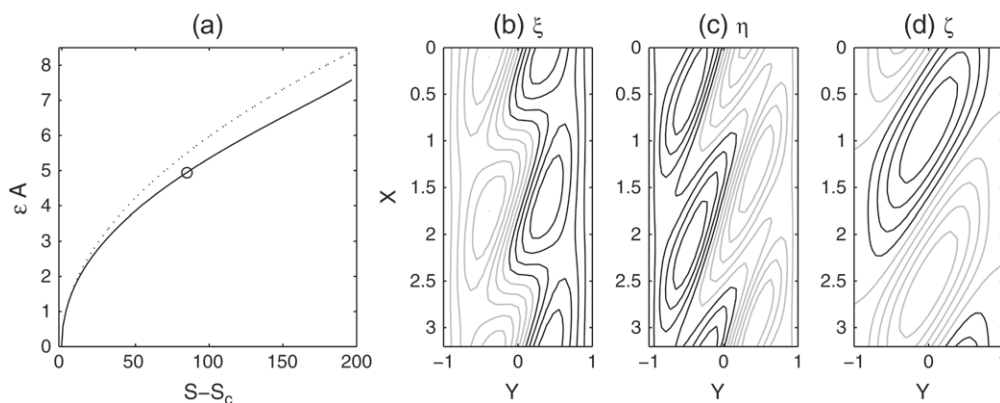

Fig. 7 Pure shear-induced buckling ($\mathcal{G} = \mathcal{T} = 0$) with $\nu = 0 \cdot 46$. Panel (a) shows the amplitude of the weakly nonlinear solution (dotted) versus that from the full numerics (solid) for the gravest ($J = 1$) buckling state. Panels (b)–(d) show $(\hat{\xi}, \hat{\eta}, \hat{\zeta})$ on the (X, Y)-plane for the $\mathcal{S}$-value indicated by the circle in panel (a). Contours are spaced by equal increments of $0 \cdot 2$ of the maximum values in each case ($12, 8 \cdot 7, 4 \cdot 9$), respectively; the lighter contours indicate negative values
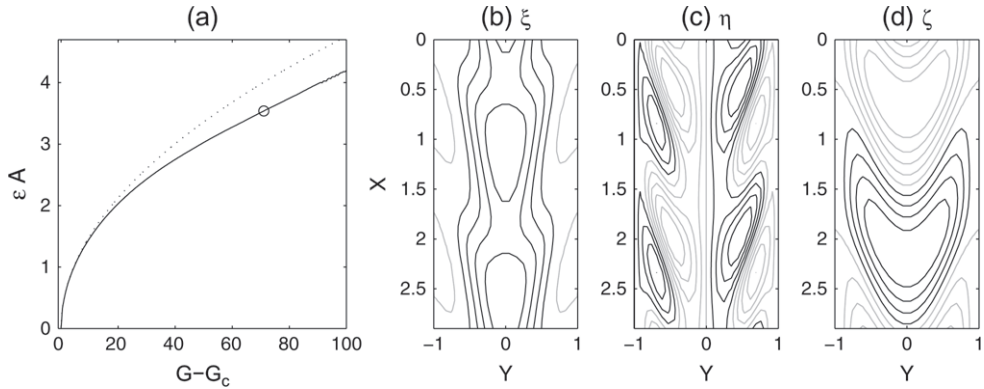
Fig. 8 Pure gravitationally induced buckling ($\mathcal{S} = \mathcal{T} = \theta = 0$) with $\nu = 0.46$. Panel (a) shows the amplitude of the weakly nonlinear solution (dotted) versus that from the full numerics (solid) for the gravest ($J = 1$) buckling state. Panels (b)–(d) show $(\hat{\xi}, \hat{\eta}, \hat{\zeta})$ on the (X, Y)-plane for the $\mathcal{G}$-value indicated by the circle in panel (a). Contours are spaced by equal increments of 0.2 of the maximum values in each case ($18.4, 4.8, 3.5$), respectively; the lighter contours indicate negative values
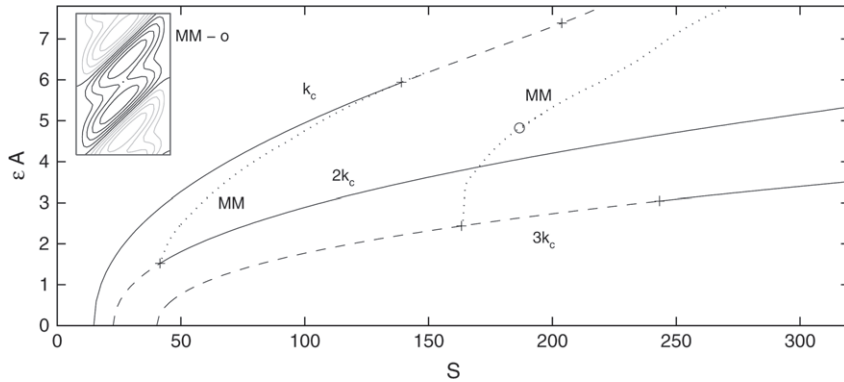

Fig. 9 The amplitudes of the first three, shear-driven buckling states ($J = 1, 2$ and 3) versus $\mathcal{S}$ with $\nu = 0.46$. The stable portions of these curves are shown by solid lines, and dashed lines where they are unstable. The crosses indicate secondary bifurcations. Two unstable connecting states with mixed character are also shown (one mixing the $J = 1$ and $J = 2$ states, the other mixing $J = 1$ and $J = 3$) and labelled MM. The inset illustrates the out-of-plane displacement of one of the mixed states (the $J = 1$ and $J = 3$ states) at the $\mathcal{S}$-value marked by the circle

$3k_c$ normal modes develop from the flat base state at $\mathcal{S} \approx 23$ and $\mathcal{S} \approx 40$, respectively, leading to the $J = 2$ and 3 finite-amplitude branches). The amplitudes along the $J = 2$ and 3 branches of the shear-driven case are compared to the primary ($J = 1$) branch in Fig. 9. Buckling states with more wavelengths in the Y-direction are also possible, but these appear at even higher values of the instability parameters.
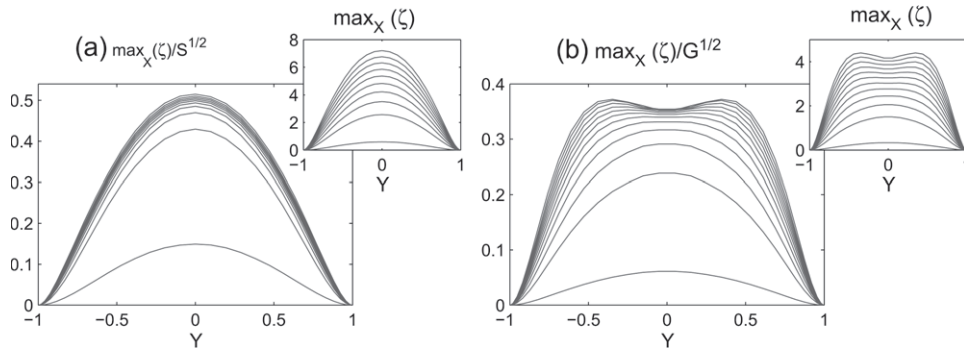
Fig. 10 Envelopes of $\hat{\zeta}$, with $\nu = 0.46$ and $\mathcal{T} = 0$, for (a) pure shear-induced buckling for $\mathcal{S}_c + 1$ up in steps of 20 and (b) pure gravitationally induced buckling for $\mathcal{G}_c + 1/2$ up in steps of 10

At larger $\mathcal{S}$ or $\mathcal{G}$, the nonlinear solutions develop features that point to a limiting behaviour. This is illustrated in Fig. 10, which shows the envelopes of the out-of-plane displacement, that is, the maximum values of $\hat{\zeta}(X, Y)$ over all X, for each Y (the silhouette of the buckling pattern when viewed in the X-direction). Displayed are the $J = 1$ envelopes for our two representative cases (pure shear and gravity). For uniform shear, the mode amplitude grows without appreciably changing shape. In the gravity case, the envelope widens with increasing $\mathcal{G}$ and eventually a double maximum develops. In either case, a scaling of the envelopes by $\mathcal{S}^{1/2}$ or $\mathcal{G}^{1/2}$, respectively, conveniently collapses the envelopes of the higher amplitude solutions onto a common curve. This rescaling implies that the bending stiffness terms are becoming negligible over the interior of the plate, and the common curve is the envelope of a nonlinear membrane solution.

Further details of a large-amplitude shear-driven buckle are shown in Fig. 11. This solution lies along the branch of the $J = 3$ buckle state and illustrates how ζ converges to the product of a Y-dependent envelope with a sinusoidal function of a variable $X - Y$ inclined at $45°$ to the coordinate axes. This observation is key to the large-$\mathcal{S}$ asymptotic analysis performed in section 6. For the gravity-driven case, a similar structure develops. Moreover, the higher J states become localized to the sheared regions at the edges of the plate, where the pattern increasingly resembles the uniform shear solutions. In other words, at large $\mathcal{G}$ and J, the gravitationally induced buckles develop in largely the same way as the shear-driven buckles, leading us to focus on the latter in the later developments.

5.2 *Secondary instabilities for uniform shear*

Because the nonlinear states described above bifurcate from the flat base state when that equilibrium first loses stability, those buckled states acquire the original stability of the base state. However, there is no guarantee that the nonlinear solutions remain stable as the instability parameter (namely, $\mathcal{S}$ or $\mathcal{G}$) is raised yet further. To complicate matters still more, although the higher order ($J > 1$) buckling states are unstable when they initially bifurcate, these states can become stable further along the solution branches as a result of secondary bifurcations. Consequently, it becomes necessary to consider the stability of the various solution branches in order to determine which are most likely to be observed.
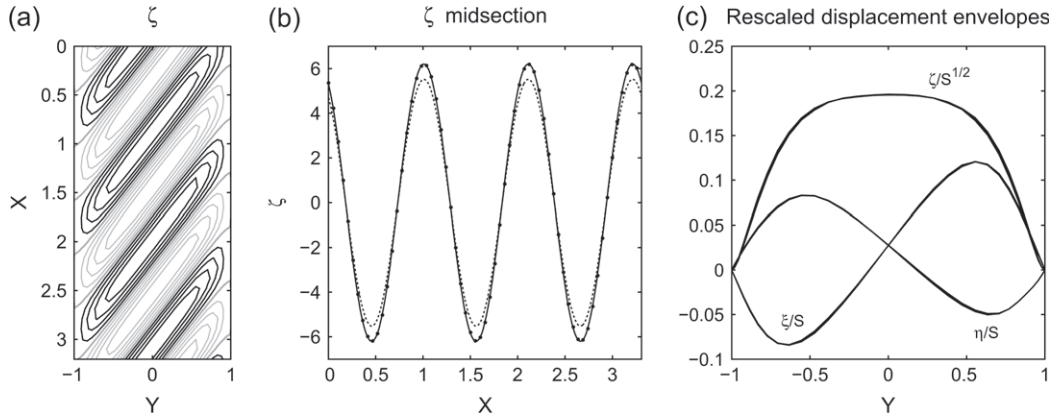
Fig. 11 The displacements for large $\mathcal{S}$: $\mathcal{S} = 1000$ and $3k_c$. Panel (a) shows the out-of-plane displacement field. Panel (b) shows the cut through the midsection ($Y = 0$) of the plate; the numerical solution is shown by the dots, a sinusoid fitted to the maxima is shown by the solid curve and the dotted curve shows the large-$\mathcal{S}$ theory. Panel (c) shows the envelopes of $\xi/\mathcal{S}$, $\eta/\mathcal{S}$ and $\zeta/\sqrt{\mathcal{S}}$ (labelled as ξ, η and ζ, respectively) for $\mathcal{S} = 600$–1000 in steps of 100

To assist in the exercise, it is useful to notice that, by judicious organization of the algebraic equations solved for the steady states, the eigenvalues of the Jacobian matrix required for the Newton–Raphson iteration determine the stability of the nonlinear solutions towards perturbations with the same periodicity. That is, the eigenvalues provide information regarding the stability of the buckled state with respect to perturbations described by Fourier sums over the wave numbers mk_c, $m = 0, 1, 2, \ldots$. Typically, one finds instabilities to be dominated by a certain wave number Mk_c, leading us to identify that instability as the 'Mth' mode (a fully fledged Floquet calculation is needed to explore stability with respect to arbitrary wave number; we opt for the simpler approach with the periodic domain).

For brevity, we focus on the shear-driven case, noting that the picture of stability for the gravity-driven buckles turns out to be qualitatively the same. The stability of the solution branches for $J = 1$, 2 and 3 is indicated by the line style in Fig. 9. The gravest ($J = 1$) buckling state remains stable upto $\mathcal{S} \approx 140$, where it loses stability to $M = 2$ modes of instability. The second buckling state is initially unstable to modes with $M = 1$ structure. At $\mathcal{S} \approx 42$, however, this state gains stability. At yet higher shears, we suspect that the $J = 2$ state loses stability again, this time towards $M = 3$ modes, but we have been unable to detect reliably this secondary bifurcation. The third ($J = 3$) branch is unstable towards $M = 1$ and $M = 2$ modes when it first appears. Successive bifurcations stabilize those modes, however, leaving the state stable for $\mathcal{S} \gtrsim 244$.

The changes of stability along the branches correspond to the appearance of secondary buckling states with mixed character, that is, states described by combinations of wave numbers. We have not traced all these secondary states required to complete the bifurcation diagram (two of the mixed branches are shown in Fig. 9 for illustration). It is clear from Fig. 9 that the higher J states gain stability before the lower branches lose stability, leading to a multiplicity of stable states at a given shear. Nevertheless, one of the key implications is that there is a pattern of bifurcations in which stability is transferred from the gravest mode to buckling states with higher and higher wave number.

A further significance of the bifurcation diagram is that, were one to gradually increase the degree of shear, there would be sudden decreases in the wavelength of the observed buckles as one tracks through the points of instability. Moreover, these transitions are hysteretic in the sense that, if one were to subsequently reduce the shear, then the shorter wavelength states would persist to smaller shears than they first appeared; eventually, they disappear in sudden lengthenings of the pattern. Note that the discontinuous changes in pattern wavelength partly result from the fixed periodic setting in which we solve the Föppl–von Kármán equations; different boundary conditions may allow smoother changes in wavelength and a more gradual shortening of the pattern with $\mathcal{S}$ or $\mathcal{G}$.

6. Strongly sheared buckles

At large shear ($\mathcal{S}$), we anticipate that the stable buckling patterns develop short wavelength in X and take an asymptotic form

$$\hat{\xi} = \mathcal{S}\Xi(Y) + \frac{\mathcal{S}}{k}\check{\xi}(U,Y), \quad \hat{\eta} = \mathcal{S}\mathcal{N}(Y) + \frac{\mathcal{S}}{k}\check{\eta}(U,Y), \quad \hat{\zeta} = \frac{\sqrt{\mathcal{S}}}{k}\check{\zeta}(U,Y), \qquad (29)$$

where $U = k(X - Y)$ and $k \gg 1$, with $\check{\xi} \sim \sin 2U$, $\check{\eta} \sim \sin 2U$ and $\check{\zeta} \sim \sin U$. Because gravitationally induced buckling at large $\mathcal{G}$ also resembles these forms, but in localized regions near the plate edges, we consider only the shear-driven case. The connection between the two large parameters $\mathcal{S}$ and k will be made explicit later in a particular distinguished limit.

In view of (29), the stresses also scale with $\mathcal{S}$, $\hat{N}_{IJ} = \mathcal{S}\check{N}_{IJ}$, and the in-plane equations become

$$\check{N}_{XX} = \nu\frac{\partial \mathcal{N}}{\partial Y} + \frac{\partial \check{\xi}}{\partial U} - \nu\frac{\partial \check{\eta}}{\partial U} + \frac{1+\nu}{2}\left(\frac{\partial \check{\zeta}}{\partial U}\right)^2 + \mathcal{O}\left(\frac{1}{k}\right), \qquad (30a)$$

$$\check{N}_{YY} = \frac{\partial \mathcal{N}}{\partial Y} + \nu\frac{\partial \check{\xi}}{\partial U} - \frac{\partial \check{\eta}}{\partial U} + \frac{1+\nu}{2}\left(\frac{\partial \check{\zeta}}{\partial U}\right)^2 + \mathcal{O}\left(\frac{1}{k}\right), \qquad (30b)$$

$$\check{N}_{XY} = \frac{1-\nu}{2}\left[\frac{\partial \Xi}{\partial Y} - \frac{\partial \check{\xi}}{\partial U} + \frac{\partial \check{\eta}}{\partial U} - \left(\frac{\partial \check{\zeta}}{\partial U}\right)^2\right] + \mathcal{O}\left(\frac{1}{k}\right) \qquad (30c)$$

and

$$\frac{\partial}{\partial U}(\check{N}_{XX} - \check{N}_{XY}) = -\frac{1}{k}\frac{\partial \check{N}_{XY}}{\partial Y}, \quad \frac{\partial}{\partial U}(\check{N}_{XY} - \check{N}_{YY}) = -\frac{1}{k}\frac{\partial \check{N}_{YY}}{\partial Y}. \qquad (31)$$

Averaging the in-plane equations over a wavelength in U yields

$$\overline{\check{N}_{XY}} = \alpha, \quad \overline{\check{N}_{YY}} = \beta, \qquad (32)$$

where an overbar indicates a U-averaged quantity and α and β are constants. Consequently,

$$\check{N}_{XX} - \check{N}_{XY} = \overline{\check{N}_{XX}} - \overline{\check{N}_{XY}} - \frac{1}{k}\int \frac{\partial \check{N}_{XY}}{\partial Y}dU, \qquad (33a)$$

$$\check{N}_{XY} - \check{N}_{YY} = \overline{\check{N}_{XY}} - \overline{\check{N}_{YY}} - \frac{1}{k}\int \frac{\partial \check{N}_{YY}}{\partial Y}dU. \qquad (33b)$$

To leading order, (33) in conjunction with (30) implies that the U-dependent part of the displacements must satisfy

$$\frac{\partial \check{\xi}}{\partial U} = -\frac{\partial \check{\eta}}{\partial U} + \mathcal{O}\left(\frac{1}{k}\right) = \frac{1}{2}\overline{\left[\left(\frac{\partial \check{\zeta}}{\partial U}\right)^2 - \left(\frac{\partial \check{\zeta}}{\partial U}\right)^2\right]} + \mathcal{O}\left(\frac{1}{k}\right) \tag{34}$$

and the mean stress components are

$$\overline{\check{N}_{XX}} \approx v\frac{\partial \mathcal{N}}{\partial Y} + \frac{1}{2}(1+v)\overline{\left(\frac{\partial \check{\zeta}}{\partial U}\right)^2}, \quad \beta = \overline{\check{N}_{YY}} \approx \frac{\partial \mathcal{N}}{\partial Y} + \frac{1}{2}(1+v)\overline{\left(\frac{\partial \check{\zeta}}{\partial U}\right)^2}, \tag{35}$$

$$\alpha = \overline{\check{N}_{XY}} \approx \frac{1}{2}(1-v)\overline{\left[\frac{\partial \Xi}{\partial Y} - \left(\frac{\partial \check{\zeta}}{\partial U}\right)^2\right]}. \tag{36}$$

Moreover, since $\mathcal{N}$ and Ξ vanish on the plate's edges, the latter conditions can be integrated over Y to find the formulae

$$\alpha \approx -\frac{1}{2}(1-v)\left\langle\left(\frac{\partial \check{\zeta}}{\partial U}\right)^2\right\rangle, \quad \beta \approx \frac{1}{2}(1+v)\left\langle\left(\frac{\partial \check{\zeta}}{\partial U}\right)^2\right\rangle. \tag{37}$$

At this stage, it is now clear that

$$\check{N}_{XY} - \check{N}_{YY} = \alpha - \beta + \mathcal{O}\left(\frac{1}{k^2}\right), \tag{38}$$

$$\check{N}_{XX} - 2\check{N}_{XY} + \check{N}_{YY} = \frac{1}{2}(1-v^2)\overline{\left(\frac{\partial \check{\zeta}}{\partial U}\right)^2} + (1+v)\beta - 2\alpha + \mathcal{O}\left(\frac{1}{k^3}\right). \tag{39}$$

These relations can be introduced into the leading-order out-of-plane equation

$$k^2(\check{N}_{XX} - 2\check{N}_{XY} + \check{N}_{YY} - 1)\frac{\partial^2 \check{\zeta}}{\partial U^2} + k[2(\check{N}_{XY} - \check{N}_{YY}) + 1]\frac{\partial^2 \check{\zeta}}{\partial U \partial Y} + \check{N}_{YY}\frac{\partial^2 \check{\zeta}}{\partial Y^2}$$

$$= \frac{1}{\mathcal{S}}\frac{\partial^2 \check{\zeta}}{\partial t^2} + \frac{4k^4}{3\mathcal{S}}\frac{\partial^4 \check{\zeta}}{\partial U^4} + \mathcal{O}\left(\frac{k^3}{\mathcal{S}}\right). \tag{40}$$

The right-hand side of (40) incorporates the leading-order time derivatives and bending stiffness terms. The former term implies that the important timescale is $O(\mathcal{S}^{-1/2})$, and an appropriate change of variable then keeps this term $O(1)$. If $k^4/\mathcal{S} \ll 1$, the latter disappears from the problem, leaving the membrane limit. For $k^4/\mathcal{S} \gg 1$, on the other hand, the bending stiffness dominates and stabilizes buckling. In the distinguished limit, $k^4/\mathcal{S} = O(1)$, both buckling and bending stiffness enter the problem, and we consider this case in detail. Though our main focus is the steady buckled states, we leave the time derivatives in (40) to facilitate a brief discussion of stability.

For the steady states, in order that the solution takes the sinusoidal-in-U form observed, the middle term on the left of (40) must cancel. Thus, we find a separable solution $\check{\zeta} = \mathcal{Z}(Y)\sin U$ along with

$$\alpha \approx -\frac{1}{4}(1-v), \quad \beta \approx \frac{1}{4}(1+v), \quad \left\langle\left(\frac{\partial \check{\zeta}}{\partial U}\right)^2\right\rangle = \frac{1}{2}\langle\mathcal{Z}^2\rangle \approx \frac{1}{2} \tag{41}$$

and

$$\frac{d^2 \mathcal{Z}}{dY} + \left[(1 - \nu)k^2 (1 - \mathcal{Z}^2) - \frac{16k^4}{3\mathcal{S}(1 + \nu)} \right] \mathcal{Z} = O(k^{-1}).$$ (42)

The left-hand side of (42) contains terms of order k^2 and unity, and a formal asymptotic procedure would then demand that we deal with them separately, giving $\mathcal{Z}^2 = 1$ everywhere. However, this solution cannot satisfy the boundary conditions at the edges of the plate. The implication is that this solution holds in the bulk of the domain and that there are boundary layers adjacent to the edges, of width k^{-1}, that have not been taken into account. Indeed, the numerical solutions reported in Fig. 11 and below support this conclusion.

To avoid dealing with these boundary layers, we take a different tack hereon. Equation (42) is formally accurate to $O(k^{-1})$; the trouble is in dealing with the left-hand side asymptotically. Instead, we follow a more qualitative approach in which we discard the error terms and solve that equation in its entirety. This is a nonlinear oscillator equation on which we impose zero displacement conditions $\mathcal{Z}(\pm 1) = 0$. Unfortunately, because not all the bending stiffness terms have been incorporated into the scheme, we cannot impose all the clamped boundary conditions. Moreover, the resulting solutions cannot satisfy the constraint $\langle \mathcal{Z}^2 \rangle = 1$ exactly, but only to $O(1/k)$.

Sample solutions to (42) are shown in Fig. 12, for the wave numbers $k = 3k_c = 5\cdot 7$ and $k = 5k_c = 9\cdot 5$. These profiles are compared with the envelopes of the out-of-plane displacement of the full numerical solution in the figure. Despite the relatively small values of k used in the comparison, the theory compares favourably with the numerical data.

Note that the asymptotic theory predicts that a solution can be found only when

$$\mathcal{S} > \mathcal{S}_c = \frac{16k^4}{3(1 + \nu)} \left[(1 - \nu)k^2 - \frac{\pi^2}{4} \right]^{-1},$$ (43)

which is a crude estimate of the stability boundary that can be compared with more accurate results given in section 3 (this estimate erroneously depends upon ν, but since this is a large-amplitude theory, it cannot be expected to remain good for the small amplitudes at onset). It also incorrectly predicts that the $J = 1$ branch does not exist, which is not surprising given that $k = k_c = 1\cdot 9$ is not large.

It is straightforward to show that the membrane solutions, with $k^4/\mathcal{S} \to 0$ in (42), are unstable: small perturbations to the buckled state with normal-mode form, $z(Y) \exp(imkX - i\omega t)$, and
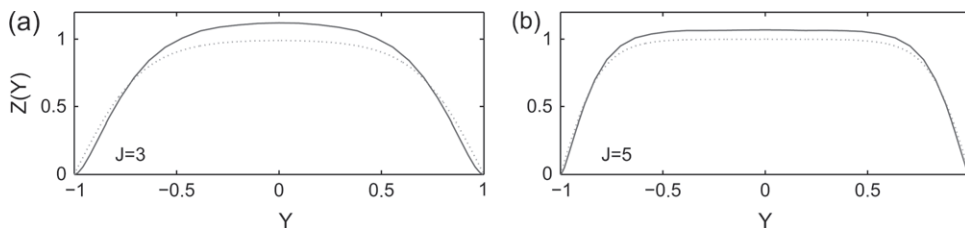

Fig. 12 Envelopes of the out-of-plane displacement for (a) $J = 3$ and (b) $J = 5$. The dotted line shows the solution of (42), and the solid curve shows the full numerical solution (for $\mathcal{S} = 2000$ in (a) and $\mathcal{S} = 5000$ in (b) with $\nu = 0\cdot 46$ in both)

different wave number ($m \neq 1$, implying that $\overline{\zeta_U^2} \to \mathcal{Z}^2$), satisfy

$$\frac{d^2 Z}{dY} + [\mathcal{M}(1 - \nu)(1 - \mathcal{Z}^2) - l]z = 0, \tag{44}$$

where $\mathcal{M} = m^2 k^2$ and $l = -4\omega^2/(1+\nu)$. For a given $l > 0$ (ω imaginary), Sturmian oscillation theory of ordinary differential equations (**18**) establishes that there is an infinite sequence of solutions with ascending values of $\mathcal{M}$. That is, for a given growth rate, one can always find a sufficiently large wave number solution, thus proving instability. Numerical solution of the linear stability problem (44) including the stiffness term (which modifies l to $l = 4/(1+\nu)[-\omega^2 + 4m^4 k^4/3\mathcal{S}]$) establishes further that one can stabilize these instabilities for $k^{-4}\mathcal{S} \sim O(1)$. In other words, one expects the stable large-$\mathcal{S}$ solutions to be characterized by wavelengths $k \sim \mathcal{S}^{1/4}$ and displacements $\zeta \sim \mathcal{S}^{1/4}$, which are the dimensionless counterparts of the scalings used by Wong and Pellegrino (**6**).

7. Uniform shear experiments

The set-up for our experimental investigation of shear-induced buckling is shown in Fig. 13. A long, slender sheet of Neoprene (polychloroprene) rubber was clamped along its longer edges (the top and bottom in Fig. 13) to aluminium slats that were held on a frame and which could be controllably sheared by turning a screw; the shorter edges of the sheet were left free (to the left and right in Fig. 13). When the sheet was initially inserted, we attempted to avoid introducing any lateral slack or tension in the sheet and clamped the edges as uniformly as was possible. To investigate a range of physical parameters, we varied the width ($2Y_0$) and thickness ($2d$) of the sheet, as well as the type of Neoprene (as measured by its durometer 'hardness' (**19**), a monotonically increasing function of the Young's modulus). The precise parameters for each experiment are listed in Table 1.

The photograph in Fig. 13 also illustrates a typical pattern obtained after sufficiently shearing the sheet. For such patterns, we estimated wavelengths along the sheet (taking the mean of several crest-to-crest distances) and measured the amplitude of the out-of-plane displacement (by using vernier calipers to gauge the crest-to-trough distance for several different buckles). In all the experiments conducted, the sheet was at least five wavelengths long, and we performed measurements in the central regions. For comparison with theory, we assume $\nu = 0.46$. As for most elastomers, the Poisson ratio of Neoprene is close to 0.5; errors associated with our choice are small compared to experimental errors.

By varying the edge displacement (imposed shear), we tracked both wavelength and amplitude as the pattern developed from its onset. For most of the experiments, the wavelength did not change
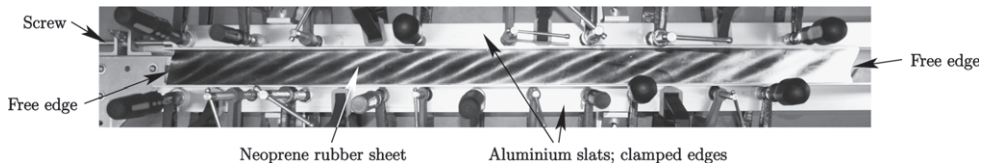

Fig. 13 A plan-view photograph of the apparatus (for Experiment 8) for shear-induced buckling. The Neoprene sheet is clamped between parallel aluminium slats mounted on a frame. The slats are at least 6 mm thick to distribute the force from each clamp. The upper support slides from left to right; visible on the left is a screw which controls the displacement

Table 1 Shear-induced buckling experiments: the experimental parameters and the symbol used in subsequent plots. The error in the half thickness, d, is $\pm 0 \cdot 05$ mm, in the half width, Y_0, is $\pm 0 \cdot 5$ mm and in the durometer is ± 5

Experiment	d/mm	Y_0/mm	Durometer	Symbol
1	0·85	47·0	50	●
2	0·85	30·7	50	+
3	0·85	23·5	50	▼
4	0·85	15·1	50	▲
5	0·85	28·5	50	◁
6	0·88	28·5	70	▷
7	1·53	24·8	70	▽
8	0·85	25·2	50	◇
9	0·85	25·0	50	□
10	1·53	25·2	70	○
11	0·85	48·3	50	△
12	0·85	50·0	50	×
12*	0·85	50·0	50	⊗

*Experiment 12 after enforced wave number doubling at large $\mathcal{S}$.
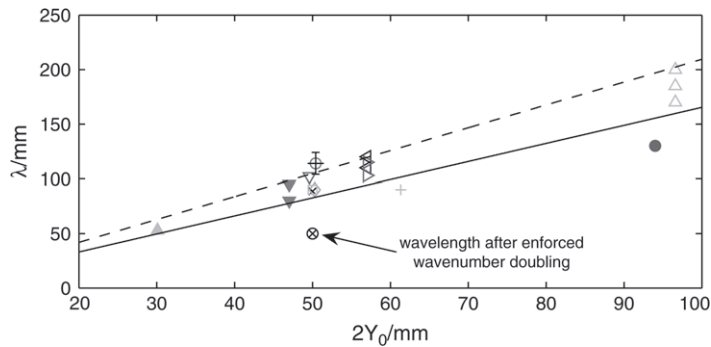

Fig. 14 The observed wavelength λ versus the width of the sheared sheet. The symbols indicate experimental data, the solid curve is the linear stability prediction of the critical wavelength at onset for $\mathcal{T} = 0$ and the dashed curve is that for $\mathcal{T} = -2$. Experimental error bars are included for a single data point

appreciably once the pattern appeared (except for Experiment 12, where we forced a wave number doubling at large shear to yield the series 12*). A collection of the results is shown in Fig. 14, which also displays the most unstable buckle wavelength expected from linear stability theory $(2\pi / k_c)$. A significant limitation of the apparatus was that it was difficult to eliminate all initial slack, with the result that there was always a slight amount of pre-compression present which could influence the buckling. For example, an inwards displacement of the edges of just 0·1 mm (almost impossible to
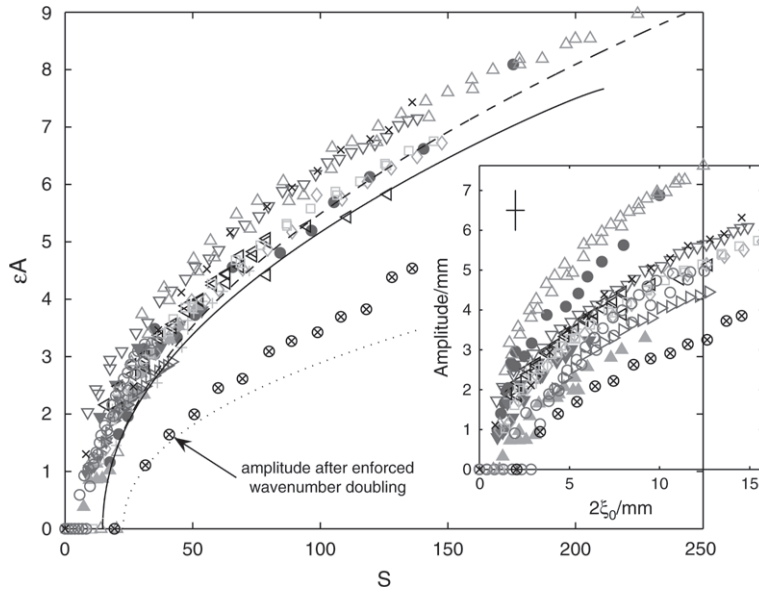
Fig. 15 The non-dimensional average amplitude of buckling versus the shear parameter $\mathcal{S}$. The curve is the prediction from weakly nonlinear theory and the solid curve that from the full numerics for the k_c mode; the dotted curve is the prediction from the full numerics for the $2k_c$ mode. The inset shows the dimensional amplitudes versus the edge displacement

eliminate) corresponds to a dimensionless compression parameter of $\mathcal{T} \approx -2$, which significantly shifts the critical wave number at onset, as illustrated in Fig. 14. Given this drawback, the agreement is tolerable between theory and experiment.

The observed out-of-plane buckle amplitudes are shown against edge displacement $2\xi_0$ in Fig. 15. The inset shows the spread of the original dimensional amplitudes; the main panel takes these data and uses theory to express the measurements in dimensionless form. Also included in the figure are the predictions of the weakly and fully nonlinear theories (with $\mathcal{T} = 0$). Another comparison of the observed buckling pattern with theory is shown in Fig. 16, which shows the envelope of the out-of-plane displacement for one example during Experiment 2.

Theory consistently overpredicts the onset and underpredicts the amplitude, but if one again allows for a small amount of pre-compression, the comparison is improved. Alternative explanations for the discrepancy are imperfections in the material (**3**, **20**) or imperfect clamping. The importance of the latter can be estimated by comparing the prediction for onset with clamped boundaries to those with simply supported boundaries ($\mathcal{S}_c = 8\cdot8$) or hinged boundaries ($\mathcal{S}_c = 9\cdot1$). However, we believe that the discrepancy is most likely due to initial slack.

Another disagreement between theory and experiment is that there are no sudden changes in wavelength as the shear is raised, unlike the predictions regarding secondary instability in section 5.2. However, the experimental shears are not sufficiently large to precipitate that instability according to Fig. 9, and the experiment is not periodic in X. A gradual decrease in wavelength was observed in Experiment 11, which achieved the highest shear values of $\mathcal{S} \approx 230$, with new crests
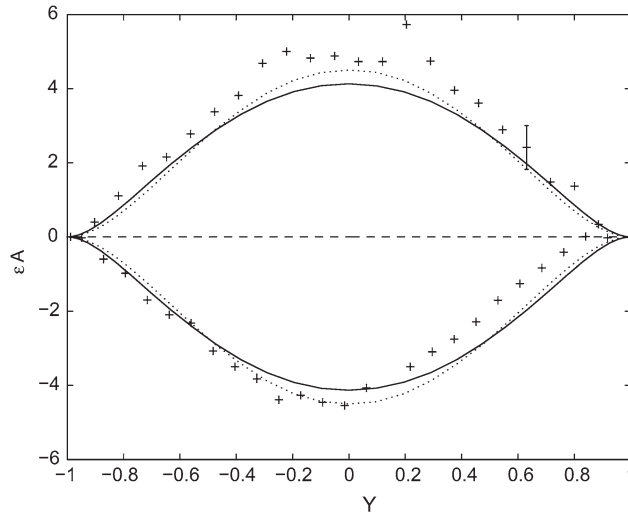
Fig. 16 The dimensionless envelope of the profile as a function of the dimensionless cross-sheet coordinate, Y, for Experiment 2 at $\mathcal{S} = 72$. The dotted curve gives the weakly nonlinear prediction and the solid curve is from the full numerics

and troughs developing at the free edges and moving inwards. To test further the ideas about secondary instability, at large $\mathcal{S}$ in Experiment 12 we looked for multiple buckle states by pressing onto the crests of the existing buckles and forcing the rubber sheet to double its wavelength (series 12*). This new pattern persisted on reduction of the shear, with the measured amplitude in tolerable agreement with that predicted for the $2k_c$ mode by the full numerics (Fig. 15). These observations resonate with the theoretical predictions, although the pattern did not revert to the k_c mode at small shear.

A final disagreement hidden in Fig. 15 is that often the path followed by the experimental amplitudes was different on ramping up in shear, compared to when the shear was ramped down, giving more than one amplitude value at each $\mathcal{S}$. Some of the hysteresis could have arisen from the apparatus 'slipping' during the increase of shear, although no such problems were evident. More likely is that some degree of permanent deformation was occurring because of the non-Hookean nature of Neoprene. Indeed, a residual pattern was often observed after running the experiment and declamping the sheet. To minimize this problem, we used a fresh piece of Neoprene for each experiment whenever possible.

8. Conclusions

Our goal in this article has been to build a picture of how nonlinear buckling patterns appear when a clamped flat plate is either sheared at its edges or subjected to a body force like gravity. To this end, we have presented linear and weakly nonlinear analyses in tandem with nonlinear computations of steady equilibria within the framework of the Föppl–von Kármán equations. We compared the theory with a simple shear experiment, finding some level of agreement. A similar comparison for gravitationally driven buckles was less successful: the gravity case requires a very large system

to observe buckling (for the Neoprene, the sheet must have a width of order 1 m and a length of the order of several metres). Though we were able to set up a large-scale experiment in which we observed folds and wrinkles in the sheet, it was impossible to avoid significant slack and non-uniformity in the initial clamping. The experimental data showed some consistency with the theory (in the way in which the buckle wavelengths scaled with the width, for example), but these were not sufficiently satisfactory to warrant its inclusion here.

The most severe drawbacks of the theory are that it is based on the Föppl–von Kármán equations. These equations have the advantage of capturing the dynamics of low-amplitude perturbations to a flat plate while retaining a relatively simple form and have been asymptotically derived from the governing equations of elasticity, incorporating geometric nonlinearity into the strains but retaining a linear constitutive model (**21**). However, the system is non-dissipative and is limited to out-of-plane displacements that must be of order the plate thickness, with the in-plane displacements smaller still. By contrast, in the experiments, perturbations to the Neoprene sheet were clearly damped relatively quickly, and the lateral shears that we imposed in order to buckle the sheet reached a similar magnitude to the out-of-plane displacement. Despite this, the theory and experiments are in tolerable agreement, leading us to believe that the theory is qualitatively applicable. In principle, one might avoid issues of this sort by attacking the problem using the full governing equations of nonlinear viscoelasticity. However, the relative simplicity of the Föppl–von Kármán equations allows one to make substantial headway in the theory, justifying the approach.

References

1. A. E. H. Love, *A Treatise on the Mathematical Theory of Elasticity*, 4th edn. (Dover, New York 1944).
2. R. V. Southwell and S. W. Skan, On the stability under shearing forces of a flat elastic strip, *Proc. R. Soc. Lond.* A **105** (1924) 582–607.
3. H. Gough and H. Cox, Some tests on the stability of thin strip material under shearing forces in the plane of the strip, *ibid.* **137** (1932) 145–157.
4. E. H. Mansfield, *The Bending and Stretching of Plates* (Cambridge University Press 1989).
5. C. D. Coman, On the applicability of tension field theory to a wrinkling instability problem, *Acta Mech.* **190** (2007) 52–72.
6. Y. W. Wong and S. Pellegrino, Wrinkled membranes part II: analytical models, *J. Mech. Mat. Struct.* **1** (2006) 27–60.
7. E. Mansfield, Gravity-induced wrinkle lines in vertical membranes, *Proc. R. Soc. Lond.* A **375** (1981) 307–325.
8. F. P. J. Rimrott and M. Cvercko, Wrinkling in thin plates due to in-plane body forces, *Inelastic Behaviour of Plates and Shells* (ed. L. Bevilacqua; Springer 1986) 19–48.
9. J. H. Fink and R. C. Fletcher, Ropy pahoehoe: surface folding of a viscous liquid, *J. Volcanol. Geotherm. Res.* **4** (1978) 151–170.

10. L. D. Landau and E. M. Lifschitz, *Theory of Elasticity* (Pergamon Press, Oxford 1970).

11. R. Huang and Z. Suo, Wrinkling of a compressed elastic film on a viscous layer, *J. Appl. Phys.* **91** (2002) 1135–1142.

12. M. Ben Amar and Y. Pomeau, Crumpled paper, *Proc. R. Soc. Lond.* A **453** (1997) 729–755.

13. Y. W. Wong and S. Pellegrino, Wrinkled membranes part I: experiments, *J. Mech. Mat. Struct.* **1** (2006) 3–26.

14. Y. W. Wong and S. Pellegrino, Wrinkled membranes part III: numerical simulations, *ibid.* **1** (2006) 61–93.

15. Y. B. Fu and R. Ogden, Nonlinear stability analysis of pre-stressed elastic bodies, *Continuum Mech. Thermodyn.* **11** (1999) 141–172.

16. Y. B. Fu, Perturbation methods and nonlinear stability analysis, Chapter 10, *Nonlinear Elasticity: Theory and Applications*, LMS Lecture Notes 283 (ed. Y. Fu and R. Ogden; Cambridge University Press 2001).

17. B. Fornberg, *A Practical Guide to Pseudospectral Methods* (Cambridge University Press 1996).

18. E. L. Ince, *Ordinary Differential Equations* (Dover, New York 1956).

19. ASTM Standard D2240-00, *Standard Test Method for Rubber Property—Durometer Hardness (Types A, B, C, D, DO, E, M, O, OO, OOO, OOO-S, and R)* (ASTM International, West Conshohocken, PA).

20. W. T. Koiter, On the stability of elastic equilibrium. Ph.D. Thesis, Technische Hooge School, Delft (transl. 1945).

21. P. G. Ciarlet, Une justification des équations de von Kármán, *C. R. Acad. Sci. Paris Sér.* A **288** (1979) 469–472.